Structural and chemical studies of the nanoscale modifications induced by swift heavy ion irradiation in SrTiO 3 at grazing incidence

Mohammad S Jamal, Victor Pierron, Tagi Tagiyev, Jérémy Blond, Stéphane Guillous, Clara Grygiel, Stéphane Flament, Bruno Guillet, Zhe Wang, Darrell G Schlom, et al.

ADVANCED FUNCTIONAL MATERIALS
www.afm-journal.de

Structural and Chemical Studies of the Nanoscale Modifications Induced by Swift Heavy Ion Irradiation in $SrTiO_3$ at Grazing Incidence

Mohammad S. Jamal, Victor Pierron, Tagi Tagiyev, Jérémy Blond, Stéphane Guillous, Clara Grygiel, Stéphane Flament, Bruno Guillet, Zhe Wang, Darrell G. Schlom, Isabelle Monnet, Laurence Méchin, and Mamour Sall**

Swift Heavy Ion (SHI) irradiation offers a powerful approach for tailoring structural and chemical properties of materials through precise energy deposition mechanisms. This study explores nanoscale structural and chemical transformations induced by SHI irradiation in $SrTiO_3$ (STO) thin films. A 20 nm STO layer, grown on a Si (001) substrate by molecular beam epitaxy, is irradiated with 71 MeV $^{129}Xe^{19+}$ ions at a grazing incidence angle of 3°. Atomic force microscopy and reflection high-energy electron diffraction reveal the formation of amorphous nanohillocks aligned with the ion tracks, exhibiting increased roughness with nanoscale ion tracks forming a ripple pattern. High-resolution scanning transmission electron microscopy combined with electron energy loss spectroscopy identifies structural phase separation within the hillocks, characterized by SrO and TiO_x segregation, along with compositional shifts, including Sr depletion and localized oxygen deficiency. Analyses of the fine structures of Ti $L_{2,3}$ and O K edges highlight oxygen vacancies and the partial reduction of Ti^{4+} to Ti^{3+} in the hillocks. These findings provide critical insights into the mechanisms of SHI-induced structural and chemical modifications, with potential implications for defect engineering and nanostructuring in oxide materials.

1. Introduction

Irradiation of solid materials with energetic particles, such as Swift Heavy Ions (SHI), induces a wide range of structural modifications depending on the material and irradiation parameters. These modifications extend from the creation of point defects to the amorphization in the bulk of the material, and the formation of nanoscale features such as hillocks and craters on the surface.[1–5] In materials sensitive to radiolysis, the underlying processes are primarily driven by energy deposition into the electronic subsystem via electronic stopping power (S_e), while nuclear stopping – direct interaction between the projectile and the nuclei plays a secondary role, contributing to localized defect formation along each ion trajectory. Critical factors such as the ion type, energy, fluence, and angle of incidence strongly influence the morphology and the extent of these changes, making SHI irradiation a powerful tool for controlling material modification. Over the past decades, SHI-induced structural changes have been extensively studied in a wide variety of materials, motivated by their relevance in nanostructuring,[6] thin-film processing,[7,8] and the development of radiation-resistant materials for technological and scientific applications.[1,9,10] In fact, the localized energy deposition along the ion trajectory may lead to permanent nanoscale structural modifications when the

M. S. Jamal, S. Guillous, C. Grygiel, I. Monnet, M. Sall
Université Caen Normandie
CEA
ENSICAEN
CNRS
Normandie Univ
CIMAP UMR6252, Caen F-14000, France
E-mail: mamour.sall@ganil.fr

The ORCID identification number(s) for the author(s) of this article can be found under https://doi.org/10.1002/adfm.202509004

DOI: 10.1002/adfm.202509004

V. Pierron, T. Tagiyev, J. Blond, S. Flament, B. Guillet, L. Méchin
Université Caen Normandie
ENSICAEN
CNRS
Normandie Univ
GREYC UMR6072, Caen F-14000, France
E-mail: laurence.mechin@cnrs.fr

Z. Wang, D. G. Schlom
Department of Material Science and Engineering
Cornell University
Ithaca, NY 14853-1501, USA

D. G. Schlom
Kavli Institute at Cornell for Nanoscale Science
Cornell University
Ithaca, NY 14853-1501, USA

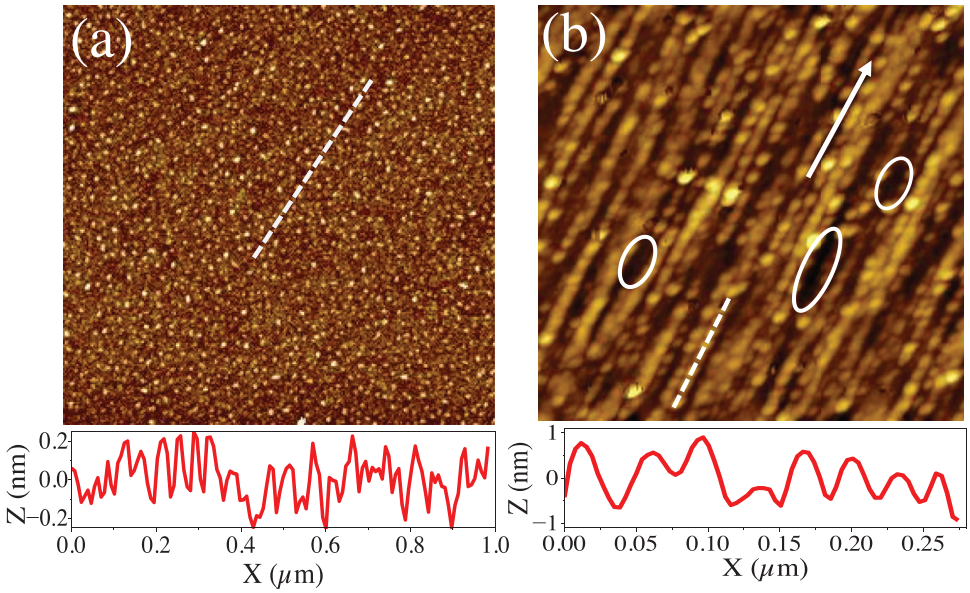

Figure 1. AFM images showing the surface morphology of a) STO (20 nm)/Si before irradiation and b) after irradiation with 71 MeV Xe ions at an angle of 3° with the surface, with a fluence of 8×10^{10} ions cm^{-2}. The arrow indicates the direction of irradiation. The scan areas are 2×2 μm^2 and 1×1 μm^2, respectively. Line profiles corresponding to the marked dashed lines in each image are displayed below, providing the surface topography and hillock height, respectively. The average period of the hillock is 37 nm along the ion tracks.

deposited energy density, i.e., S_e, is sufficiently high to transiently melt the material on a picosecond timescale.[5,11] Subsequently, the molten region, surrounded by a cold matrix, undergoes a rapid quenching process, forming a highly disordered or amorphous ion track.[11–13] Near the material surface, the high pressure within the melted region can be released by a protrusion toward the surface of melted matter along the ion trajectory.[6,13,14] Therefore, surface nanostructures could be created and, in fact, have been achieved with the observation of nano-hillocks and craters using irradiation geometries ranging from normal to oblique and grazing incidence, offering flexibility in tailoring surface morphologies.[2,3,13,15,16] For instance, at grazing incidence SHI irradiation, discontinuous nano-hillocks form at the surface of materials along the ion beam direction, resulting in chain-like nano-hillocks.[5,15] These chain-like structures, characterized by their high degree of periodicity and alignment, present promising opportunities for applications and have been reported in various oxide materials, including $SrTiO_3$ (STO),[8,17] $LaMnO_3$,[8] InSnO,[9], etc. In particular, STO, a perovskite with unique electronic and optical properties, has gained renewed interest. STO is valued for its large dielectric constant, transparency, and compatibility with other perovskites, making it a suitable substrate for growing microelectronic heterostructures and a model system for ferroelectricity studies.[18,19] Consequently, in recent decades, the STO substrate has been extensively utilized as a model system for investigating defect engineering under SHI irradiation, leading to nanoscale, morphological, structural, and chemical transformations. Crespillo et al. demonstrated that oxygen vacancies in $SrTiO_3$ can be unambiguously identified via a distinct red luminescence emission at ≈2.0 eV, which originates from Ti^{3+} polarons trapped at isolated oxygen vacancy sites.[20,21] This spectral signature offers a robust diagnostic for tracking vacancy formation and enables precise defect engineering in perovskite oxides through ion beam irradiation. Recent research has demonstrated the formation of self-organized wave-like structures on the STO surface under grazing incidence SHI irradiation,[6] as well as the development of core–shell structures under normal incidence, featuring an amorphous core surrounded by a disordered crystalline shell.[17,22] These investigations have significantly advanced our understanding of SHI-induced structural transformations in STO. However, while the physical processes and microstructural characteristics of ion tracks are well documented, the chemical states and compositional analyses of these features remain poorly characterized, limiting the full use of these modifications for practical applications. In fact, despite their potential, the application of SHI-induced nanostructures remains limited compared to low-energy ion-beam sputtering techniques.[7,23–26] Yet, the ability to fine-tune at the nanoscale ion track density through fluence adjustments and to control track length by modifying ion energy or angle of incidence highlights the versatility of SHI for advanced surface engineering.[6]

In this study, we integrate nanoscale structural analyses with chemical characterization to bridge the gap in the current understanding of SHI-induced modifications at the surface of STO thin films. The insights gained from this study contribute to the broader knowledge of ion-beam-driven material transformations and highlight the applicative potential of tailored nanostructuring in perovskite systems.

2. Morphological Properties of SHI Irradiated STO

Atomic Force Microscopy (AFM) images in **Figure 1** provide critical insights into the morphological evolution of the STO thin film surface, before and after SHI irradiation. The pristine STO sample exhibits a homogenous and smooth surface, characterized by

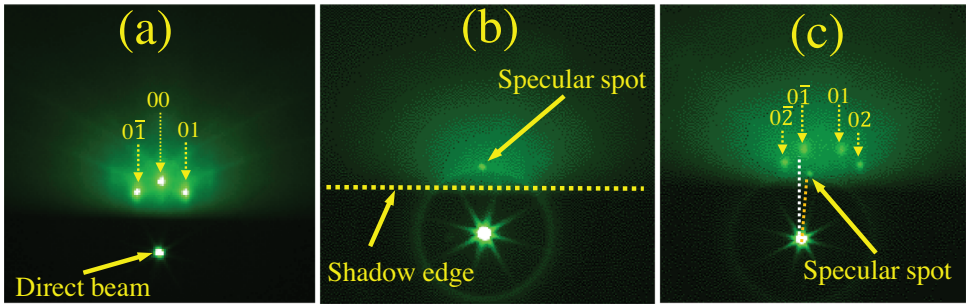

Figure 2. RHEED patterns of a) nonirradiated STO(001) and b,c) irradiated STO surfaces, captured with the electron beam aligned (b) perpendicular and (c) parallel to the SHI irradiation direction.

a root-mean-square (RMS) roughness below 0.5 nm across the 2 × 2 μm^2 scan area. The line profile along the white dashed line in Figure 1a reveals minor height variations between −0.25 and 0.25 nm, consistent with high-quality epitaxial growth and minimal surface irregularities for STO. However, postirradiation, the surface morphology undergoes a significant transformation, as depicted in Figure 1b. The irradiated sample exhibits chains of nano-hillocks aligned with the ion irradiation direction as previously reported in [5,9] (see profile in Figure 1b). With the irradiation fluence of 8×10^{10} ions.cm^{-2}, the chains of nano-hillocks are predominantly interconnected in the irradiation direction. They are interspersed with regions of nonirradiated surface, marked by white ellipses in Figure 1b, in the direction perpendicular to the chains. The RMS roughness increases to ≈1.5 nm, reflecting the surface's nanoscale restructuring due to SHI-induced modifications. Along a given ion direction, the average periodicity of the nano-hillock chains is 37 nm, which is lower than the literature value of 58 nm for nanohillocks aligned along the [100] crystallographic direction for irradiations with similar macroscopic S_e than in the present study.[5] The reduction in periodicity compared to literature values can be attributed to the ion beam's deviation from the [100] crystallographic axis, which reduces the electronic stopping power and alters the energy dissipation pattern. This correlation between periodicity and crystallographic alignment supports the notion that structural modifications are strongly influenced by the orientation of the irradiation direction relative to the crystal lattice.

The nanoscale surface restructuring is confirmed by the Reflection High-Energy Electron Diffraction (RHEED) measurements. For the nonirradiated STO surface (**Figure 2**a), the RHEED pattern was recorded with the electron beam aligned along the [100] crystallographic axis of STO. The pattern exhibits bright spots corresponding to the 0$\bar{1}$, 00, and 01 diffraction peaks, indicative of a well-ordered crystalline surface.[27] In the irradiated sample, when the electron beam is perpendicular to the chain of hillocks (Figure 2b), only a specular reflection spot is observed. This indicates a loss of long-range crystalline order at the surface with possible amorphization. Conversely, when the electron beam is aligned parallel to the chain of hillocks (Figure 2c), weak diffraction spots (0$\bar{2}$, 0$\bar{1}$, 01, and 02) become visible. These features suggest the coexistence of nonirradiated crystalline regions embedded among the disordered chains of hillocks.[23] The diffraction pattern corresponds to the [100] crystallographic axis of STO.[27] Interestingly, the central 00 peak is not observed in Figure 2c. Upon closer inspection, the specular reflection and diffraction spots appear tilted to the right relative to the straight dashed white line. This asymmetry in the diffraction pattern indicates that the nano-hillock chains deviate from perfect alignment with the [100] crystallographic direction. Attempts to obtain a symmetric diffraction pattern by rotating the sample were unsuccessful, confirming that the asymmetry arises due to the alignment of the nano-hillock chains deviating from the [100] crystallographic axis. This misalignment corroborates the AFM observations of reduced periodicity in the nano-hillock chains, further emphasizing the influence of the irradiation geometry on surface morphology.

The structural quality of the STO layer and its interface with silicon was examined closely using Transmission Electron Microscopy (TEM) and High-Angle Annular Dark Field Scanning TEM (HAADF-STEM) prior to the irradiation process as shown in **Figure 3**. The magnified images of TEM (Figure 3b) and HAADF-STEM (Figure 3d) reveal the epitaxial growth of the crystalline STO layer on the Si substrate. Fast Fourier Transform (FFT) patterns, presented to the right of Figure 3b for selected regions, confirm the presence of well-ordered domains in the STO layer oriented along the growth direction. A thin amorphous SiO_2 layer (≈2 nm) was observed at the interface between the STO layer and the Si substrate. This layer forms due to oxygen diffusion through STO during growth, resulting in the oxidation of silicon beneath the STO. Notably, this process does not disrupt the crystal structure of the first few atomic layers of the epitaxially grown STO.[28]

The HAADF-STEM images in **Figure 4** provide a detailed nanoscale perspective of the structural changes induced by SHI irradiation, complementing the surface morphological and crystallographic information obtained through AFM and RHEED. The postirradiation HAADF-STEM image (Figure 4) in cross-sectional configuration, in a projection view perpendicularly to the direction of the chains of hillocks, highlights amorphous hillocks (red dashed circles) on the STO surface and irregular amorphous regions (red dashed squares) within the STO layer. These latter features confirm that the SHI-induced energy deposition effect extends beyond the surface, penetrating into the STO layer and inducing localized amorphization. This is consistent with the S_e value of $^{129}Xe^{19+}$ 71 MeV ion in STO (19 keV nm^{-1}) which is higher than the S_e threshold value (12.7 keV nm^{-1} [29]) for the creation of discontinuous track in bulk STO and of chains of hillocks at its top surface.

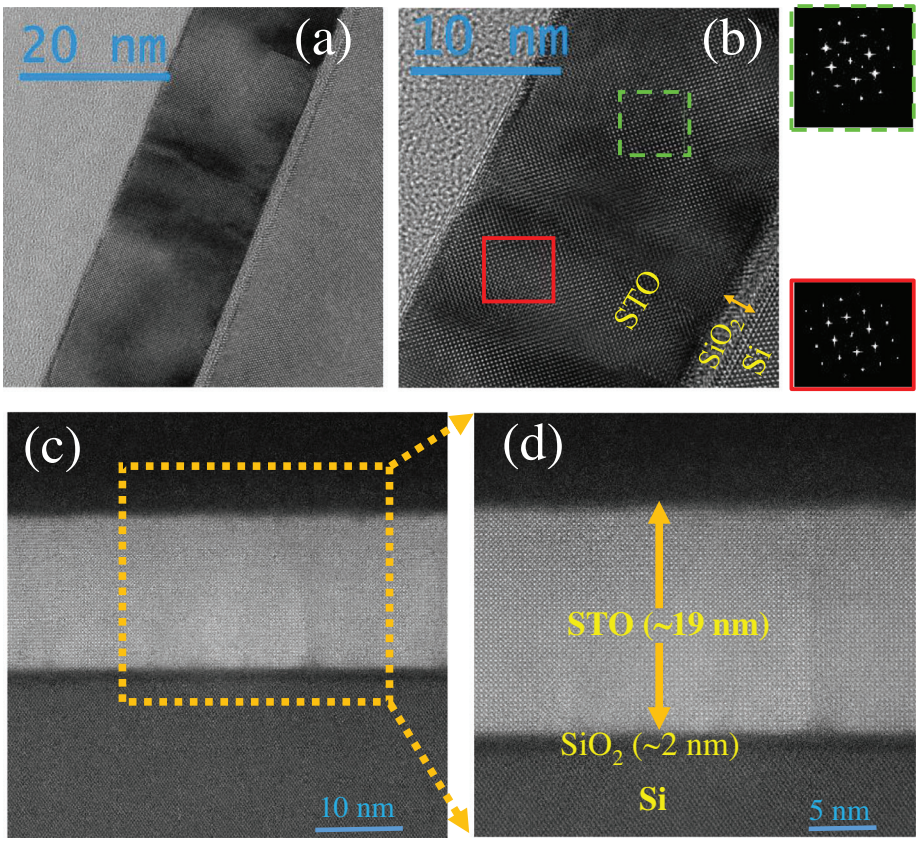

Figure 3. a) HR-TEM image and c) HAADF-STEM image of the STO (20 nm)/Si sample. The corresponding magnified images b) and d) provide a detailed view of the STO, SiO_2, and Si layers, clearly distinguishing the crystalline regions (Si and STO) from the amorphous SiO_2 layer. The FFT patterns from square regions indicated in (b) are shown on the right, offering insights into the structural quality and domain orientation of the STO layer.

The structural analysis combining RHEED measurements and high-resolution HAADF-STEM imaging clearly reveals the amorphous character of the SHI-created hillocks at the surface of STO. This brings new insights into the morphology of SHI-induced surface nanostructures of STO that has been extensively studied.[2,5,6,9,13,29] However, in these previous studies, there is a lack of information concerning the chemical composition of the hillocks. This could limit the understanding of the physical mechanism behind the evolution of these hillocks after a particular treatment like thermal annealing,[9] chemical etching,[1,9] or supplemental SHI irradiation with fluence where ion tracks overlap.[6] In this paper, we have studied the chemical composition in the hillock utilizing STEM-EELS spectroscopy with a particular emphasis on the Ti and O fine structures in order to probe their local bonding environments.

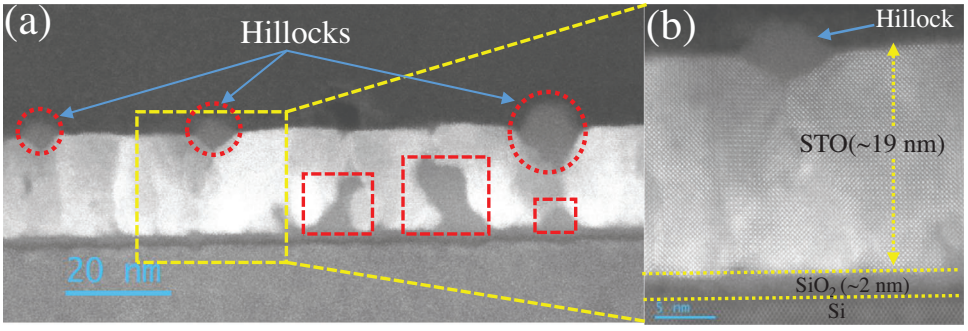

Figure 4. a) HAADF-STEM image of the STO (20 nm)/Si sample irradiated with 71 MeV Xe^{19+} ions at a grazing incidence angle of 3°, showing the formation of amorphous hillocks (highlighted by red dashed circles) and irregular amorphous regions (marked with red dashed squares). b) High-resolution HAADF STEM image of the region outlined by the yellow dashed rectangle in (a), offering a detailed view of a single hillock. This image clearly differentiates the crystalline regions (Si and STO) from the amorphous areas, including SiO_2, and the hillock structure.

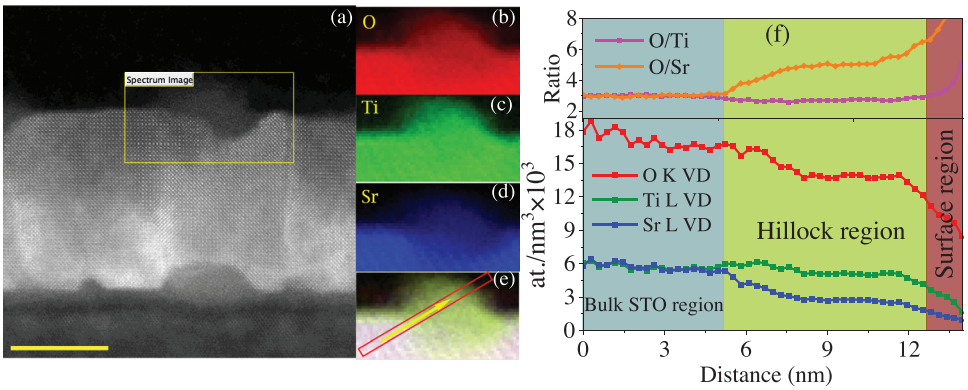

Figure 5. a) HAADF-STEM image of the irradiated STO (20 nm)/Si sample, highlighting a single hillock. b–d) EELS mapping for the O K, Ti $L_{2,3}$, and Sr $L_{2,3}$ edges within the region outlined by the yellow rectangle in (a). e) Combined RGB elemental map for the same area, with O represented in red, Ti in green, and Sr in blue. f) EELS volumetric density profile for O, Ti, and Sr extracted from the red rectangular area in (e) along the yellow arrow, as shown at the bottom of (f). The ratios of O/Ti and O/Sr, are displayed at the top of (f), providing a quantitative analysis of elemental distribution.

3. Chemical Analysis of the Hillock

Figure 5a presents the results of chemical analysis of a hillock by means of Electron Energy Loss Spectroscopy (EELS) measurements. The elemental maps (see Figure 5c,d) for oxygen, titanium, and strontium show a noticeable reduction in Sr and O content relative to Ti content within the hillock, compared to the bulk STO region where the composition is near the nominal ratio O:Sr:Ti of 3:1:1 (Figure 5f). The loss of Sr in the surface hillock could be due to the higher volatility of SrO in comparison to TiO_x. In fact, Sr has a lower enthalpy of evaporation (141 kcal mol^{-2}) compared to Ti (427 kcal mol^{-1}) and a lower boiling point (1653 vs 3533 K).[30] The loss of Sr probably happened during the transient melting and the mass transport toward the surface along the ion trajectory as explained in the introduction part.

Besides the depletion of Sr inside the hillock, the EELS chemical maps at the atomic scale (pixel size: 0.05 nm × 0.05 nm and probe size: < 0.08 nm) in **Figure** 6 reveal the separation of the phases SrO and TiO_x within the hillock region as displayed by dashed orange and blue regions in color mixed Ti+Sr image. The intensity profile (for red rectangle in color mix O+Ti+Sr) of the EELS maps in Figure 6b indicates alternating ≈0.5 nm-wide Sr-rich and Ti-rich regions within the hillock, while the periodicity of Sr, Ti, and O atomic columns is well-defined in the non-disordered part of the material. To further elucidate the nature of these hillocks and understand the phase separation into SrO and TiO_x a detailed EELS fine-structure analysis was performed.

4. Ti and O Fine Structures

As illustrated in **Figure** 7, EELS was utilized to probe the chemical environment in two distinct regions: the crystalline STO layer (black circle in Figure 7a) and the amorphous hillock (red circle in Figure 7a). The corresponding EELS spectra shown in Figure 7b, reveal notable differences in the fine structure of the Ti $L_{2,3}$ edge between these regions. In the crystalline STO layer (black curve), the Ti $L_{2,3}$ fine structure exhibits four well-defined peaks at specific energy loss values: t_{2g} (L_3) at 456.86 eV, e_g (L_3) at 459.11 eV, t_{2g} (L_2) at 462.22 eV, and e_g (L_2) at 464.43 eV. The characteristic four-peak structure of the Ti $L_{2,3}$ edge results from transitions from Ti $2p_{3/2}$ states to the unoccupied Ti 3d t_2g and Ti 3d e_g states, followed by transitions from Ti $2p_{1/2}$ states to Ti 3d t_{2g} and Ti 3d e_g states. The alignment of these peak positions with recent literature [31] confirms the expected electronic structure of bulk $SrTiO_3$ and validates the spectral data. In contrast, the Ti $L_{2,3}$ fine structure in the amorphous hillock (red curve) shows a distinct shift in the e_g (L_2) and e_g (L_3) peaks toward lower energy by ≈0.45 eV. This energy shift indicates a reduced oxidation state of Ti within the hillock, suggesting the presence of oxygen vacancies and/or a modification in the local bonding environment due to the amorphous character of the hillock.[32,33] This is also consistent with the oxygen deficiency in the hillock revealed by the composition analysis presented in Figure 5.

The EELS data of the O-K edge were obtained from three distinct regions: Area A (bulk STO), Area B (hillock), and Area C (hillock), as illustrated in **Figure** 8a. In Figure 8b, in the bulk STO region, the O-K edge energy range is divided into two regimes based on electronic transitions involving hybridized oxygen orbitals. The first regime (525–539 eV) reflects shape-resonances arising from two main transitions: i) transitions from O 1s → O 2p↔Ti 3d hybridized orbitals, giving rise to peak a (Ti 3d t_{2g}) at 530 eV and peak b (Ti 3d e_g) at 532.6 eV, and ii) transitions from O 1s → O 2p↔Sr 4d hybridized orbitals, producing peak c (Sr 4d e_g) at 534.5 eV and peak d (Sr 4d t_{2g}) at 536 eV. These well-defined features arise from the strong crystal field splitting caused by the octahedral coordination of oxygen atoms around Ti and Sr in the perovskite structure.[34] The observed splitting between peaks a and b is 2.61 eV, characteristic of bulk STO with fully oxidized Ti^{4+}, consistent with previously reported high-resolution O-K edge spectra for STO.[31,34,35] The second regime (539–560 eV) shows broader shape-resonances corresponding to transitions from O 1s → Ti 4sp orbitals, labeled as peak e. The intensity and width of this peak reflect the hybridization of Ti 4sp and O 2p orbitals. Significant spectral changes are observed in the hillock region compared to the bulk STO spectrum. Peaks a and b for the spectra in the hillock, corresponding to O 2p → Ti 3d (t_{2g}, e_g) transitions, broaden and merge, with their separation reduced from 2.61 to 1.85 eV, indicating a reduced crystal field strength in the hillock. This reduction in splitting aligns with reported values for trivalent oxides such as Ti_2O_3, V_2O_3,

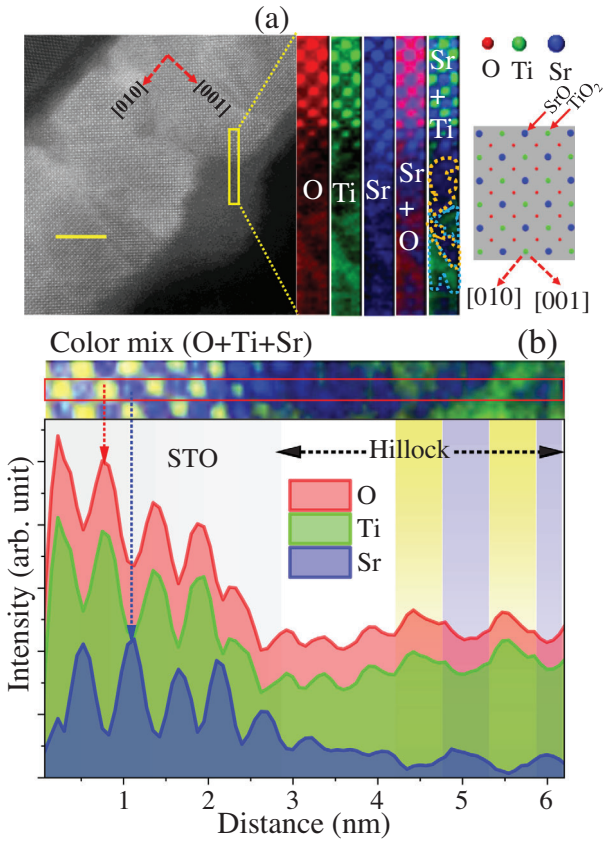

Figure 6. a) Overview HAADF-STEM image of the irradiated STO (20 nm)/Si sample along the [100] crystallographic direction, with the area marked by a yellow rectangle selected for high-resolution elemental mapping. The corresponding elemental maps display the spatial distributions of O (red), Ti (green), and Sr (blue), followed by composite maps of Sr+O and Sr+Ti. The light blue and orange dashed line regions in the Sr+Ti composite represent SrO-rich and TiO_x-rich regions, respectively. On the far right, a simulated structural model replicates the observed atomic arrangement, illustrating alternating SrO and TiO_2 planes along the [001] growth direction. b) The HAADF signal intensity profile was extracted from the red rectangular region in the top mixed-color (O+Ti+Sr) image. The corresponding intensity plot, shown at the bottom, highlights the atomic column positions of O, Ti, and Sr, as indicated by the arrows.

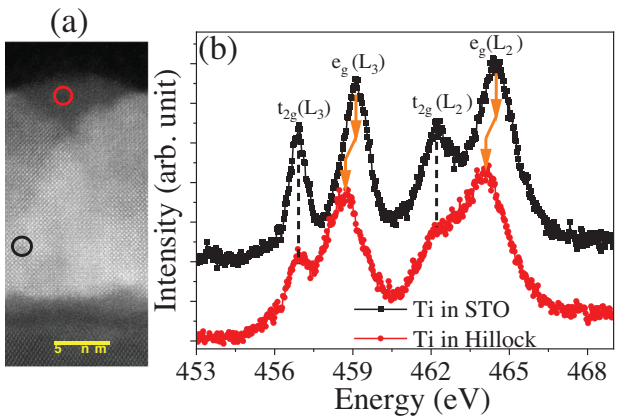

Figure 7. a) HAADF-STEM images highlighting the spectrum acquisition points: within the crystalline STO region (black circle) and the amorphous hillock (red circle). b) Corresponding Ti $L_{2,3}$ edge fine structures for the STO region (black line with solid square) and hillock (red line with solid circle), showing distinct spectral features.

Cr_2O_3, Mn_2O_3, and Fe_2O_3 where crystal field splitting typically ranges from 1.8 to 2.0 eV.[35] This strongly suggests that Ti^{4+} in the bulk STO has been partially reduced to Ti^{3+} in the hillock due to oxygen deficiency, consistent with the Ti-$L_{2,3}$ edge analysis discussed earlier. Peaks c and d, associated with Sr 4d contributions, are significantly reduced at position B in the hillock, indicating Sr depletion in the hillock region, consistent with the elemental line profile analysis shown in Figure 5f. In contrast, at position C in the hillock, peaks c and d merge into a single peak with a slight shift toward higher energy, suggesting a reduction in the crystal field strength. The appearance of this single peak in one spectrum and its absence in the other hillock spectrum indicates the coexistence of SrO-rich and SrO-depleted regions within the hillocks. This observation aligns with high-resolution STEM data, where phase separation of SrO and TiO_x was discussed.

The evolution of Ti oxidation states from bulk STO to the amorphous hillock was examined in detail using EELS mapping, as illustrated in **Figure 9**. A rectangular mapping region (yellow rectangle) was chosen to encompass both crystalline STO and the amorphous hillock (Figure 9a). Figure 9b shows the Ti $L_{2,3}$ edge fine structure (hollow circles) collected from the red-circled region in (a), encompassing both crystalline STO and the amorphous hillock. The spectrum was analyzed using Multiple Linear least squares (MLLS) fitting through the Gatan Digital Micrograph environment. The fitting results decomposed the spectra into contributions from Ti in crystalline STO (black line) and Ti in the amorphous hillock (red line), with the blue curve representing the total fit. The e_g ($L_{2,3}$) peaks of Ti fit in the hillock exhibited a consistent shift toward the lower energy side by 0.45 eV, confirming a reduced oxidation state in the hillock region relative to bulk STO. The MLLS fitted maps (Figure 9c) show the change of Ti oxidation state in the entire hillock. To further investigate the gradual evolution of Ti oxidation states, EELS Ti $L_{2,3}$ edges were collected pixel-by-pixel (pixel size: 0.51 nm × 0.51 nm) along a 10.5 nm length rectangular region marked in Figure 9e. The Ti-$L_{2,3}$ edge spectra (Figure 9f) reveal peak broadening and less pronounced peak splitting of e_g and t_{2g} in the hillock region, consistent with the decrease of oxygen coordination with Ti either due to O deficiency and/or amorphous character of the hillock.[32,33] The degree of broadening and reduced splitting increases from the STO/hillock interface to the surface.

To quantify the oxygen deficiency (δ) in $SrTiO_{3-\delta}$ with a precision of 1% in the oxygen-deficient region (hillock), the parameter $R = \frac{I(e_g(L_3))-I_0}{I(t_{2g}(L_3))-I_0}$ was calculated, as it is directly correlated with oxygen vacancy concentration.[36,37] Here, I_0 represents the intensity at the valley point between the e_g (L_3) and t_{2g} (L_3) peaks. A higher R-value indicates a greater degree of oxygen deficiency. Figure 9g presents the spatial distribution of the R-value for each pixel within the selected yellow region in Figure 9a, obtained by computing the intensity amplitudes $e_g(L_3)$, $t_{2g}(L_3)$, and I_0. This analysis provides a detailed mapping of oxygen deficiency across the crystalline STO and amorphous hillock regions, revealing

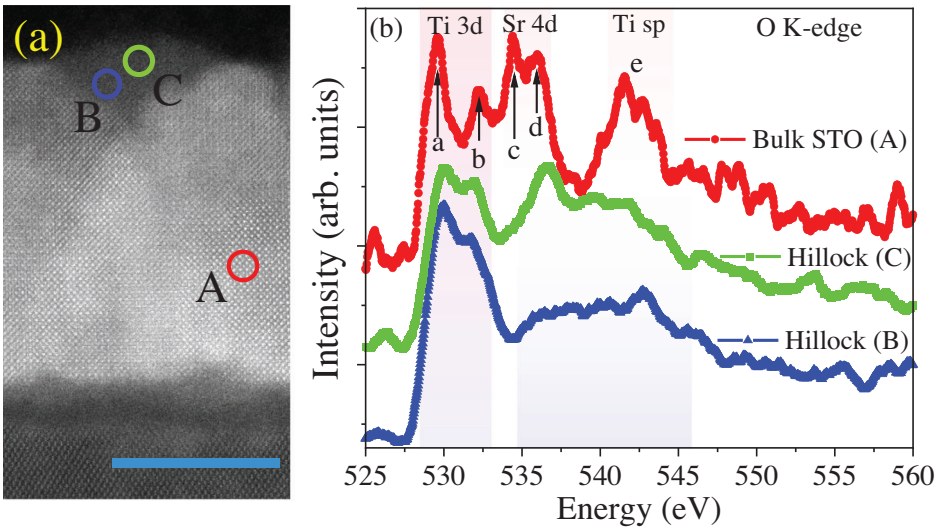

Figure 8. HAADF-STEM image of the irradiated STO (20 nm)/Si sample, highlighting positions A, B, and C representing EEL spectra of the O-K edge from Area A (bulk STO, red curve) and Area B and C (hillock, green, and blue curves).

localized stoichiometric and chemical state variations induced by irradiation. Notably, the hillock region appears predominantly white, indicating a higher oxygen deficiency than the bulk STO region. Figure 9h illustrates the variation of the R-value along the yellow arrow in Figure 9g, showing an exponential increase with distance along the line profile. The experimentally observed R-values at distances of 4.76 nm (interface region) and 7.42 nm (near the hillock surface) are 2.92 and 11.84, respectively, as marked by arrows in Figure 9h. By comparing the experimentally obtained R-values with literature data,[36] the corresponding contributions of Ti^{3+} (X) and Ti^{4+} (Y) with X + Y = 1, which are directly related to the oxygen deficiency (δ), can be determined. Specifically, the analysis of the reported R-values in [37] allows for the estimation of X, yielding values of ≈0.1 for R = 2.92 (interface region) and ≈0.46 for R = 11.84 (hillock surface). Since each oxygen vacancy in $SrTiO_{3-\delta}$ generates two Ti^{3+} ions, the oxygen deficiency δ is given by $\delta = X/2$. Thus, the calculated δ-values for the interface region and near the hillock surface are 0.05 and 0.23, respectively, indicating a significant increase in oxygen deficiency toward the surface.

The observed reduction of Ti^{4+} to Ti^{3+} due to oxygen deficiency along with the depletion of Sr content and the phase separation of SrO and TiO_x within the hillocks could be understood by considering the transient high temperature (thermal spike) produced by SHI along its path. The rapid melting/boiling and quenching processes favor oxygen out-diffusion, leading to localized vacancies within the hillocks. These vacancies destabilize the Ti^{4+} oxidation state, resulting in a partial reduction to Ti^{3+}. Such reductions have also been observed in TiO_2 nanorods under SHI where strain and defect formation were reported to modify electronic properties with the change of the bandgap from direct to indirect at high fluence levels.[38] The transient high temperatures facilitate preferential evaporation or displacement of Sr atoms, while the higher stability of Ti ensures minimal variation in its content between the hillocks and the bulk STO. Such preferential evaporation is analogous to the findings in 2D MoS_2 layers, where S vacancies form due to the lower sublimation temperature of S relative to Mo.[39] Similarly, in STO, the disparity in the enthalpy of evaporation could explain the selective depletion of Sr from the hillocks. The phase separation of SrO and TiO_x within the hillocks is another consequence of the thermal spike. The difference in evaporation enthalpies and bonding characteristics of Sr and Ti results in the segregation of these phases during resolidification. The rapid cooling traps the separated phases within the hillock structure, as evidenced by the compositional maps and structural analyses. Comparable behavior has been reported in the literature, where thermal annealing of STO and titanium oxides at temperatures above 850 °C leads to film decomposition, including SrO desorption and the formation of distinct oxide phases.[9,40,41]

5. Conclusion

This comprehensive investigation of swift heavy ion-irradiated $SrTiO_3$ thin layers at grazing incidence highlights, for the first time, significant material decomposition into nano-hillocks created at the surface of the material. These nano-hillocks present an amorphous structure and phase separation of SrO and TiO_x. Quantitative EELS analysis showed oxygen deficiency and Sr depletion in the hillock in comparison to the crystalline bulk $SrTiO_3$. The analysis of the fine structures of both titanium and oxygen revealed an important reduction of titanium from Ti^{4+} to Ti^{3+} due to oxygen deficiency. These results advance our understanding of ion-beam-induced modifications in perovskite systems and underscore the potential of SHI irradiation for tailoring the properties of oxide materials for technological applications, including radiation-resistant devices and nanostructured components.

6. Experimental Section

Material: A 20 nm thick epitaxial $SrTiO_3$ (STO) film was grown on a Si (001) substrate using molecular beam epitaxy. The growth process

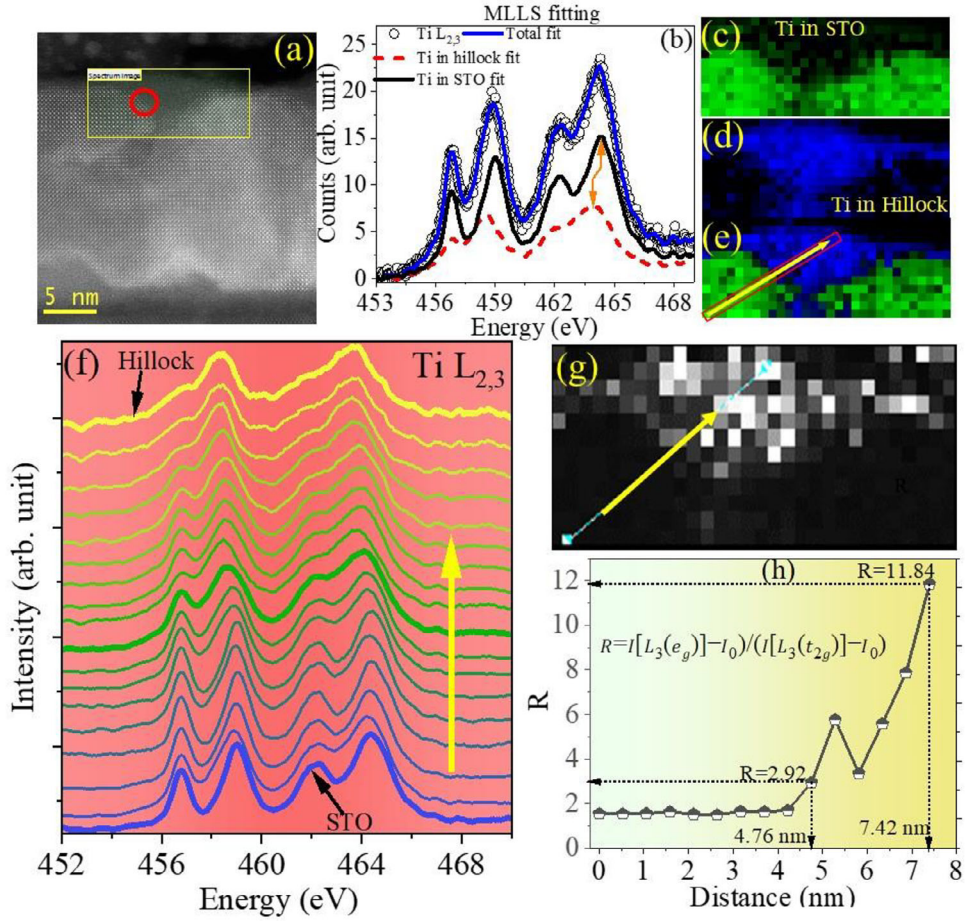

Figure 9. a) HAADF-STEM image of the irradiated STO (20 nm)/Si sample, highlighting a single hillock. The yellow rectangle indicates the region selected for spectrum imaging to analyze the Ti fine structure. b) Ti $L_{2,3}$ edge fine structure (hollow circles) collected from the red-circled region in (a), encompassing both crystalline STO and the amorphous hillock. The spectrum was analyzed using Multiple Linear Least Squares (MLLS) fitting, with contributions from Ti in crystalline STO (black line) and Ti in the amorphous hillock (red line). The blue curve represents the total fit for the spectrum. c–e) Mapping of MLLS fit coefficients: (c) Ti in crystalline STO, (d) Ti in the hillock, and (e) a composite map combining (c) and (d). (f) EELS Ti $L_{2,3}$ edges were collected pixel-by-pixel (pixel size: 0.51 nm × 0.51 nm) along the arrow for the rectangular region marked in (e). The arrow indicates the direction of extracted spectra from STO to an amorphous hillock. The spectra for bulk STO, the interface, and surface evolution points with different oxidation states are highlighted by thicker lines. (g) Parameter $R = \frac{I(e_g(L_3))-I_0}{I(t_{2g}(L_3))-I_0}$ calculated using MLLS fitting for the yellow rectangular region by calculating the intensities $I(e_g(L_3))$, $I(t_{2g}(L_3))$, *and* I_0 where we set the intensity for the valley point between e_g (L_3) and t_{2g} (L_3) as I_0. (h) Parameter R plotted as a function of distance along the marked arrow in (g).

employs a kinetically controlled deposition technique as described in previous studies.[42,43] This method ensures high-quality epitaxial growth with precise stoichiometric control and minimizes defect formation.

Irradiation: The STO thin films were irradiated at the IRRSUD ion beamline of GANIL (Caen, France) using $^{129}Xe^{19+}$ ions with an energy of 71 MeV, having a S_e value of 19 keV nm^{-1} in STO, calculated using the SRIM software.[44] Irradiation was performed at room temperature and at a grazing incidence angle around 3° under vacuum better than 5×10^{-5} mbar. The ion fluence was fixed at 8×10^{10} ions cm^{-2} to induce dense but near-separated nanostructures at the surface.

AFM Measurements: The AFM measurements were conducted in non-contact mode under ambient conditions using a Park Systems, Inc. (South Korea) AFM equipped with cantilevers operating in the 200–400 kHz resonant frequency range. The acquired AFM images were processed and analyzed using Gwyddion software (version 2.66).[45]

RHEED Measurements: RHEED measurements, using a setup from Staib Instruments, Inc. (Germany), were performed to investigate the structural features of the STO surface. A 30 keV electron beam with an emission current of 1.55 A was directed at the surface at a grazing incidence angle of approximately 4° during the measurements.

TEM, HAADF-STEM, and EELS Analysis: TEM experiments were performed on a double-corrected JEOL ARM 200F equipment operating at 200 kV, equipped with a GIF Quantum Gatan energy filter. A HAADF detector was used with inner and outer angles of 68 and 280 mrad, respectively. EELS experiments were performed in dual-EELS mode for elemental analysis using a Gatan K3 detector with an energy dispersion of either 0.9 or 0.03 eV/channel for higher resolution. The STEM micrographs and the EELS data were acquired and processed under the Gatan Digital Micrograph environment.

TEM Sample Preparation with the FIB Technique: TEM sample preparation in cross-sectional configuration was carried out by FIB technique with a 30 keV Ga^+ Ion Beam in a Helios Nanolab 660 system (Thermofisher). The beam current was decreased in several steps from 21 nA to 80 pA for the milling of the sample. A final cleaning step was performed with the FIB voltage decreasing gradually to 2 and 1 keV with currents of 23 and 28 pA, respectively. A protective carbon layer (≈30 nm thick) was

deposited on the STO surface before FIB milling to preserve the surface features and facilitate lamella preparation. A thick platinum (Pt) layer was subsequently deposited at the top of the carbon layer to protect the sample during milling. The FIB cross-section lamella was cut perpendicular to the grazing irradiation direction.

Acknowledgements

This work was partially supported by the ANR funding "Investissements d'avenir" ANR-11-EQPX-0020 (Equipex GENESIS), the Region Normandie through the program "Normandie Recherche – RIN Emergent»" (Project "MELIORATION" Grant No. 23E02602) and PULVECHAMP project, and by the CNRS Federation IRMA – FR 3095. The authors would like to thank P. Boduch and A. Domaracka for their help during the irradiations. The experiments were performed at the Grand Accélérateur National d'Ions Lourds (GANIL) by means of the CIRIL Interdisciplinary Platform, part of CIMAP laboratory, Caen, France. The authors thank the staff of CIMAP-CIRIL and GANIL for their invaluable support.

Conflict of Interest

The authors declare no conflict of interest.

Data Availability Statement

The data that support the findings of this study are available from the corresponding author upon reasonable request.

Keywords

AFM, grazing incidence irradiation, nano-hillocks, $SrTiO_3$, STEM-EELS, swift heavy ions, Ti oxidation states

Received: April 9, 2025
Revised: June 13, 2025
Published online: June 23, 2025

[1] E. Gruber, L. Bergen, P. Salou, E. Lattouf, C. Grygiel, Y. Wang, A. Benyagoub, D. Levavasseur, J. Rangama, H. Lebius, B. Ban-D'Etat, M. Schleberger, F. Aumayr, *J. Phys. Condens. Matter* **2018**, *30*, 285001.
[2] N. Ishikawa, T. Taguchi, N. Okubo, *Nanotechnology* **2017**, *28*, 445708.
[3] N. Ishikawa, T. Taguchi, H. Ogawa, *Quantum Beam Sci.* **2020**, *4*, 43.
[4] R. Nongjai, S. Khan, H. Ahmed, I. Khan, S. Annapoorni, S. Gautam, H. Lin, F. Chang, K. Hwa, K. Asokan, *J. Magn. Magn. Mater.* **2015**, *394*, 432.
[5] E. Akcöltekin, S. Akcöltekin, O. Osmani, A. Duvenbeck, H. Lebius, M. Schleberger, *New J. Phys.* **2008**, *10*, 053007.
[6] R. Rahali, H. Lebius, A. Benyagoub, E. Gardes, S. Guillous, I. Monnet, M. Sall, M. P. Chauvat, D. Marie, C. Grygiel, *Materialia* **2023**, *27*, 101696.
[7] A. K. Bera, D. Kumar, *ACS Appl. Electron. Mater.* **2020**, *2*, 3686.
[8] B. E. Matthews, M. Sassi, C. Barr, C. Ophus, T. C. Kaspar, W. Jiang, K. Hattar, S. R. Spurgeon, *Nano Lett.* **2021**, *21*, 5353.
[9] M. Karlušić, M. Mičetić, M. Kresić, M. Jakšić, B. Šantić, I. Bogdanović-Radović, S. Bernstorff, H. Lebius, B. Ban-d'Etat, K. Žužek Rožman, J. H. O'Connell, U. Hagemann, M. Schleberger, *Appl. Surf. Sci.* **2021**, *541*, 148467.
[10] R. Sachan, E. Zarkadoula, X. Ou, C. Trautmann, Y. Zhang, M. F. Chisholm, W. J. Weber, *ACS Appl. Mater. Interfaces* **2018**, *10*, 16731.
[11] N. Itoh, D. M. Duffy, S. Khakshouri, A. M. Stoneham, *J. Phys. Condens. Matter* **2009**, *21*, 474205.
[12] M. Toulemonde, W. Assmann, C. Dufour, A. Meftah, C. Trautmann, *Nucl. Instruments Methods Phys. Res. Sect. B Beam Interact. Mater. Atoms* **2012**, *277*, 28.
[13] F. Aumayr, S. Facsko, A. S. El-Said, C. Trautmann, M. Schleberger, *J. Phys. Condens. Matter* **2011**, *23*, 393001.
[14] O. Ochedowski, O. Osmani, M. Schade, B. K. Bussmann, B. Ban-Detat, H. Lebius, M. Schleberger, *Nat. Commun.* **2014**, *5*, 3913.
[15] E. Akcöltekin, T. Peters, R. Meyer, A. Duvenbeck, M. Klusmann, I. Monnet, H. Lebius, M. Schleberger, *Nat. Nanotechnol.* **2007**, *2*, 290.
[16] M. Lang, F. Djurabekova, N. Medvedev, M. Toulemonde, C. Trautmann, *Compr. Nucl. Mater. Second Ed.* **2020**, *1*, 485.
[17] A. K. Gupta, E. Zarkadoula, M. Ziatdinov, S. V. Kalinin, V. R. Paduri, J. A. Hachtel, Y. Zhang, C. Trautmann, W. J. Weber, R. Sachan, *Nanoscale* **2024**, *16*, 14366.
[18] C. H. Ahn, J. M. Triscone, J. Mannhart, *Nature* **2003**, *424*, 1015.
[19] P. Perna, D. Maccariello, F. Ajejas, R. Guerrero, L. Méchin, S. Flament, J. Santamaria, R. Miranda, J. Camarero, *Adv. Funct. Mater.* **2017**, *27*, 1.
[20] M. L. Crespillo, J. T. Graham, F. Agulló-López, Y. Zhang, W. J. Weber, *Appl. Mater. Today* **2018**, *12*, 131.
[21] M. L. Crespillo, J. T. Graham, F. Agulló-López, Y. Zhang, W. J. Weber, *J. Phys. D. Appl. Phys.* **2017**, *50*, 155303.
[22] X. Han, E. Zarkadoula, Q. Huang, M. L. Crespillo, X. Wang, P. Liu, *Nano Today* **2022**, *46*, 101612.
[23] A. Kumar Bera, S. Singh, M. Shahid Jamal, Z. Hussain, V. R. Reddy, D. Kumar, *J. Magn. Magn. Mater.* **2022**, *544*, 168679.
[24] K. V. Sarathlal, D. Kumar, A. Gupta, *Appl. Phys. Lett.* **2011**, *98*, 12.
[25] M. O. Liedke, M. Körner, K. Lenz, M. Fritzsche, M. Ranjan, A. Keller, E. Čižmár, S. A. Zvyagin, S. Facsko, K. Potzger, J. Lindner, J. Fassbender, *Phys. Rev. B* **2013**, *87*, 024424.
[26] Y. Yen, Y. Wang, Y. Chen, H. Tsai, F. Hu, S. Lin, Y. Chen, C. Lai, W. Liu, T. Wang, H. Hong, Y. Chueh, *ACS Appl. Mater. Interfaces* **2014**, *6*, 8327.
[27] B. Sohn, C. Kim, *J. Korean Phys. Soc.* **2022**, *81*, 1250.
[28] W. Guo, A. B. Posadas, A. A. Demkov, *J. Appl. Phys.* **2020**, *127*, 055302.
[29] M. Karlušić, S. Akcöltekin, O. Osmani, I. Monnet, H. Lebius, M. Jakšić, M. Schleberger, *New J. Phys.* **2010**, *12*, 043009.
[30] B. Mondal, T. Mukherjee, N. W. Finch, A. Saha, T. A. P. M. Z. Gao, T. DebRoy, *Materials* **2023**, *16*, 50.
[31] V. Begum-Hudde, T. Lojewski, N. Rothenbach, B. Eggert, A. Eschenlohr, K. Ollefs, M. E. Gruner, R. Pentcheva, *Phys. Rev. Res.* **2023**, *5*, 013199.
[32] A. Ohtomo, D. A. Muller, J. L. Grazul, H. Y. Hwang, *Nature* **2002**, *419*, 378.
[33] G. Bertoni, E. Beyers, J. Verbeeck, M. Mertens, P. Cool, E. F. Vansant, G. Van Tendeloo, *Ultramicroscopy* **2006**, *106*, 630.
[34] N. Palina, A. Annadi, T. C. Asmara, C. Diao, X. Yu, M. B. H. Breese, T. Venkatesan, Ariando, A. R, *Phys. Chem. Chem. Phys.* **2016**, *18*, 13844.
[35] F. Frati, M. O. J. Y. Hunault, F. M. F. De Groot, *Chem. Rev.* **2020**, *120*, 4056.
[36] Y. Li, Q. Wang, M. An, K. Li, N. Wehbe, Q. Zhang, *Adv. Mater. Interfaces* **2016**, *3*, 1600201.
[37] D. A. Muller, N. Nakagawa, A. Ohtomo, *Nature* **2004**, *430*, 657.
[38] S. Dey, A. Chakravorty, S. B. Mishra, N. Khatun, A. Hazra, B. R. K. Nanda, C. Sudakar, D. Kabiraj, S. C. Roy, *Nanoscale Adv.* **2022**, *4*, 241.
[39] L. Madauß, I. Zegkinoglou, H. Vázquez Muiños, Y. W. Choi, S. Kunze, M. Q. Zhao, C. H. Naylor, P. Ernst, E. Pollmann, O. Ochedowski, H. Lebius, A. Benyagoub, B. Ban-D'Etat, A. T. C. Johnson, F. Djurabekova, B. Roldan Cuenya, M. Schleberger, *Nanoscale* **2018**, *10*, 22908.
[40] L. V. Goncharova, D. G. Starodub, E. Garfunkel, T. Gustafsson, V. Vaithyanathan, J. Lettieri, D. G. Schlom, *J. Appl. Phys.* **2006**, *100*, 1.

[41] Y. Mizuno, F. K. King, Y. Yamauchi, T. Homma, A. Tanaka, Y. Takakuwa, T. Momose, *J. Vac. Sci. Technol. A* **2002**, *20*, 1716.
[42] M. P. Warusawithana, C. Cen, C. R. Sleasman, J. C. Woicik, Y. Li, L. F. Kourkoutis, J. A. Klug, H. Li, P. Ryan, L. Wang, M. Bedzyk, D. A. Muller, L. Chen, J. Levy, D. G. Schlom, *Science* **2009**, *324*, 367.
[43] H. Li, X. Hu, Y. Wei, Z. Yu, X. Zhang, R. Droopad, A. A. Demkov, J. E. Jr, K. Moore, W. Ooms, J. Kulik, P. Fejes, H. Li, X. Hu, Y. Wei, Z. Yu, X. Zhang, R. Droopad, A. A. Demkov, J. Edwards, *J. Appl. Phys.* **2003**, *93*, 4521.
[44] J. F. Ziegler, SRIM—The Stopping and Range of Ions in Matter **2013**, http://www.srim.org/.
[45] D. Nečas, P. Klapetek, *Cent. Eur. J. Phys.* **2012**, *10*, 181.